Applied Spectroscopy

www.s-a-s.org

SAGE

Extended Multiplicative Signal Correction for Infrared Microspectroscopy of Heterogeneous Samples with Cylindrical Domains

Ilia L. Rasskazov[1] , Rajveer Singh[2,3], P. Scott Carney[1], and Rohit Bhargava[2,4]

Abstract

Optical scattering corrections are invoked to computationally distinguish between scattering and absorption contributions to recorded data in infrared (IR) microscopy, with a goal to obtain an absorption spectrum that is relatively free of the effects of sample morphology. Here, we present a modification of the extended multiplicative signal correction (EMSC) approach that allows for spectral recovery from fibers and cylindrical domains in heterogeneous samples. The developed theoretical approach is based on exact Mie theory for infinite cylinders. Although rigorous Mie theory implies utilization of comprehensive and time-consuming calculations, we propose to change the workflow of the original EMSC algorithm to minimize extensive calculations for each recorded spectrum at each iteration step. This makes the modified EMSC approach practical for routine use. First, we tested our approach using synthetic data derived from a rigorous model of scattering from cylinders in an IR microscope. Second, we applied the approach to Fourier transform IR (FT-IR) microspectroscopy data recorded from filamentous fungal and cellulose samples with pronounced fiber-like shapes. While the corrected spectra show greatly reduced baseline offsets and consistency, strongly absorbing regions of the spectrum require further refinement. The modified EMSC algorithm broadly mitigates the effects of scattering, offering a practical approach to more consistent and accurate spectra from cylindrical objects or heterogeneous samples with cylindrical domains.

Introduction

Fourier transform infrared (FT-IR) microscopy and spectroscopic imaging[1] are commonly used to understand molecular composition in a variety of samples. Recent applications include examples from biology,[2–6] materials science,[7–9] forensics,[10,11] agriculture,[12,13] and medicine.[14–25] Although FT-IR microspectroscopy includes the exceptional molecular selectivity of fundamental absorption modes, high spectral accuracy from interferometric measurements, and robust signal-to-noise (S/N) ratios, spectral distortions[26] arise from scattering at interfaces[27] that can complicate the analysis of recorded data. For analytical measurements of samples whose sizes are comparable to the wavelength of impinging electromagnetic radiation, in practice, scattering from the object dominates the total recorded attenuation.

There is now an emerging understanding of the physics underlying spectral distortions associated with scattering of IR radiation from samples with spherical,[28,29] cylindrical,[30]

[1]The Institute of Optics, University of Rochester, Rochester, NY, USA
[2]Beckman Institute for Advanced Science and Technology, University of Illinois at Urbana-Champaign, Urbana, IL, USA
[3]Department of Civil, Architectural and Environmental Engineering, Drexel University, Philadelphia, PA, USA
[4]Departments of Bioengineering, Electrical & Computer Engineering, Chemistry, Chemical and Biomolecular Engineering, and Mechanical Science and Engineering, Cancer Center at Illinois, University of Illinois at Urbana-Champaign, Urbana, IL, USA

Corresponding author:
Rohit Bhargava, University of Illinois at Urbana-Champaign, Urbana, IL, USA.
Email: rxb@illinois.edu

thin film,[31–37] or more complex geometry.[38–40] The forward problem of predicting IR spectra, given the shape and properties of the sample, is now generally well described for a variety of cases. Various theoretical solutions of the inverse problem, namely recovering the absorption of the sample as well as its morphologic properties, for the case of single spheres[41–43] and cylinders[30] as well as for thin film samples[44,45] have been proposed. A modification of the experimental setup for minimization of recorded scattering has been also developed.[46] Theoretical approaches require either the knowledge of the particle's size,[30] or multiple[41] or even quite accurate[42,43] measurements of IR spectrum of the intact object. Though, in most cases, a single measurement of the sample with a number of spherical or cylindrical inclusions like overlapping or quite densely packaged cells[28] or fibers[47] without clear knowledge of the object size will likely occur. Therefore, for most cases, the inverse problem remains a challenging task.

A post-acquisition computational approach to address this need has been proposed. Termed extended multiplicative signal correction (EMSC),[48] this technique has been developed extensively during the last decade[49–54] for samples with spherical inclusions. It was shown that so-called dispersion artefact,[28] or effect of scattering from interfaces in which profile of the real part of the refractive index affects the recorded absorbance, can be mitigated with this algorithm. Extended multiplicative signal correction-corrected data with minimized contribution of undesirable scattering make it possible to adequately analyze IR spectroscopic data acquired from biological cells and tissues.[23,55] The applicability of EMSC thus far, however, is limited to objects with spherical shape. While the approach is effective, it is also limiting since the spherical symmetry may obscure effects that arise in other geometries. For example, many objects commonly measured by IR microscopy are cylindrical in shape (e.g., fibers, single crystals, and fungi) but an ideal cylinder as a scattering shape for EMSC has not been reported. Although the forward and inverse problems for a single intact fiber with known size are well-known,[30] a general formulation of the EMSC algorithm for cylinders and, particularly, its application to large data sets without a priori knowledge of cylinder size or refractive index is needed. Here we seek to fulfill this need by first theoretically extending the EMSC model to cylindrical geometries. Second, and in conjunction, we seek to formulate a computational strategy to work with large imaging data sets. Finally, we evaluate the efficacy of the developed approach for different samples.

Theory

Extended Multiplicative Signal Correction

We closely follow the formalism for EMSC thoroughly discussed in the references.[48,56–58] According to this algorithm,

the recorded signal $\vec{Z}_{\mathrm{Raw}}$ can be decomposed as follows:

$$\vec{Z}_{\mathrm{Raw}} = c + m\vec{\tilde{\nu}} + h\vec{Z}_{\mathrm{Ref}} + \sum_{i=1}^{7} \vec{g}_i p_i + \vec{E} \tag{1}$$

where c is the constant offset, m is the gradient of the sloping baseline, $\vec{\tilde{\nu}}$ is the wavevector (inverse wavelength λ^{-1}), h is the multiplicative scaling factor for reference signal $\vec{Z}_{\mathrm{Ref}}$, p_i and $\vec{g}_i$ are loadings and controlling parameters, respectively, for the scattering contribution, and, finally, $\vec{E}$ is an unmodelled residual information.

The recorded spectrum can be corrected by finding values of c, m and h using a least squares linear regression model. The Mie-type scattering contribution is contained in loadings p_i which are calculated from decomposition of simulated scattering efficiency Q_{sca} curves using a non-mean-centered principal component analysis (PCA). Scattering efficiency Q_{sca} is calculated at each iteration step for each recorded signal $\vec{Z}_{\mathrm{Raw}}$. Usually, up to 1000 permutations of Q_{sca} are required for an adequate estimation of p_i which arise from variations of particle size and refractive index.[50] Utilization of the appropriate expression for Q_{sca} makes it possible to adjust the EMSC approach to particles with various shapes. Conceptually, using the scattering efficiency Q_{sca} in Eq. 1 rather than the originally proposed[50] extinction efficiency Q_{ext} is a different yet reliable way to implement the EMSC.[51] Though, in Bassan et al.[50] it is assumed that under van de Hulst approximation,[59] the scatterer is non-absorbing and, as a consequence, $Q_{\mathrm{ext}} = Q_{\mathrm{sca}}$.

Scattering from Cylindrical Objects

In most cases, the longitudinal dimension (i.e., length) of natural or synthetic fibers is much larger than the transverse (diameter) dimension.[60,61] Further, the image pixel size of a typical IR microspectroscopy setup is usually comparable to the diameter of a fiber. Consequently, the ends of the fiber have little influence on any pixel towards the center and fibers can be generally approximated with an infinite cylinder for the development of a scattering model. In the case of unpolarized illumination, the scattering efficiency of an infinite cylinder embedded in a host medium with refractive index n_h can be found as:

$$Q_{\mathrm{sca}} = \frac{1}{2}\left[Q_{\mathrm{sca},\,\parallel} + Q_{\mathrm{sca},\,\perp}\right] \tag{2}$$

where

$$Q_{\mathrm{sca},\,\parallel} = \frac{2}{x}\left[|b_{0,\parallel}|^2 + 2\sum_{l=1}^{\infty}\left(|b_{l,\parallel}|^2 + |a_{l,\parallel}|^2\right)\right] \tag{3}$$

$$Q_{\text{sca}, \perp} = \frac{2}{x} \left[|a_{0,\perp}|^2 + 2 \sum_{l=1}^{\infty} \left(|a_{l,\perp}|^2 + |b_{l,\perp}|^2 \right) \right] \quad (4)$$

are longitudinal and transverse scattering efficiencies per unit length of an infinite cylinder. Here $x = 2\pi n_h \nu r$ is a dimensionless size parameter and l is the order of a spherical harmonic. Coefficients a_l and b_l in Eqs. 3 and 4 for illumination parallel $\|$ and orthogonal $\perp$ to the cylinder axis of symmetry are given in the Appendix. While we do not discuss polarized illumination and oriented fibers in this study focused on method development, the approach presented here can be extended to those two cases as well by considering cylinder and molecular orientation with respect to beam polarization.

Utilization of Eqs. 2–4 may be computationally expensive. Thus, GPU-enabled calculations[51] or implementation of simplified analytical solutions like the original[50] or modified[54] van de Hulst approximation,[59] which have been successfully applied for spherical samples, are alternative ways to estimate Q_{sca}. It should be understood, however, that in the case of cylinder, there is no adequate analytical approximation which is valid for a wide range of x. The Rayleigh approximation[59] is valid only for $x \ll 1$, which is usually not the case for micronsized objects under mid-IR illumination. Therefore, the use of Eqs. 2–4 is inevitable and the optimization of the EMSC performance becomes a crucial problem to solve.

Numerical Results

Scattering from Spheres and Cylinders

We start with a comparative analysis of scattering from single spherical and cylindrical particles. Although it is intuitive that the scattering patterns are different for these two shapes, it is worthwhile to discuss briefly the main features of each and the major differences between these two cases. The main purpose of this comparative analysis is to show the necessity of introduction of modified Resonant Mie Scattering (RMieS)/EMSC approach for the case of fibers. As a reference material, we chose polymethyl methacrylate (PMMA) whose experimentally measured spectra agree well with simulated ones.[40,41,43] Real and imaginary parts of the refractive index of PMMA are shown in Fig. 1a, while a schematic representation of illumination and scattering from the sphere and cylinder is shown in Fig. 1b and 1c.

Figure 1 explicitly shows that PMMA spheres and cylinders with the same radius r scatter electromagnetic waves in a different manner. For example, the scattering efficiency of a cylinder may be smaller, greater, or comparable with a sphere in $\nu > 2000 \, \text{cm}^{-1}$ spectral region, depending on the size of the particles. However, for sufficiently large particles, the scattering pattern is qualitatively, and in some cases quantitatively, the same in the fingerprint region, $\nu < 2000 \, \text{cm}^{-1}$. This coincident correspondence may explain the success of the EMSC approach in handling
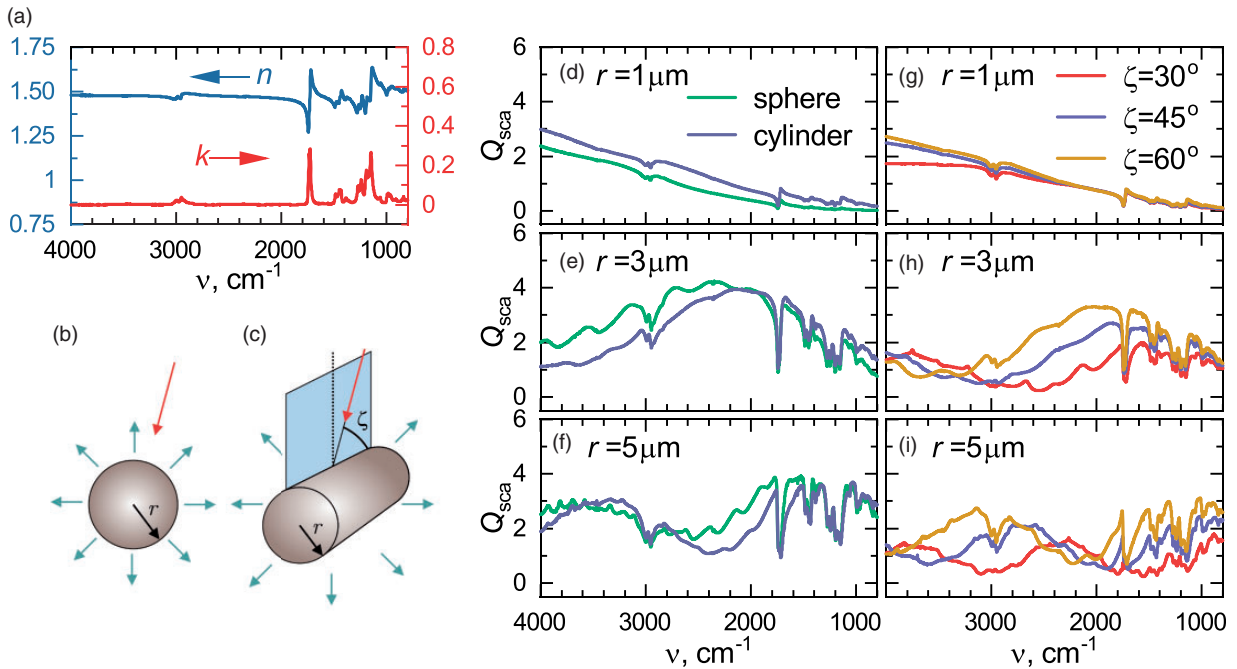

Figure 1. (a) Real, n, and imaginary, k, parts of the refractive index of bulk PMMA, and schematic representation of illumination and scattering from sphere (b) and cylinder (c) with radius r. (d–f) Scattering efficiencies Q_{sca} for spherical and cylindrical PMMA particles for various radii r. Cylinders are illuminated with unpolarized illumination under the normal incidence, $\zeta = 90°$. (g–i) Scattering efficiencies Q_{sca} for PMMA cylinders with different radii r illuminated under various angles ζ.

materials that are not spherical as well; however, the differences demonstrate that the geometry must be considered for precise mitigation of scattering effects.

Unlike the sphere, the fiber is an object with rotational symmetry, thus Q_{sca} also depends on the polarization of the incident illumination and spatial orientation of the fiber with respect to it. As an approximation when polarizers are not specifically used, IR spectroscopy utilizes unpolarized illumination. Thus, only the angle of incidence ζ gives rise to the additional degree of freedom which has to be included to permutations of Q_{sca} along with refractive index n_p and radius r. For polarized electromagnetic wave and/or molecularly oriented cylindrical samples, further modifications may be added to these permutations. Figure 1 shows that the scattering pattern of a cylinder strongly depends on the diameter as well. For relatively small cylinders ($r = 1\mu m$), the scattering pattern is very similar for small wavenumbers (longer wavelengths compared to the radius) and varies quantitatively for different ζ. In contrast, for a relatively large ($r = 5\mu m$) cylinder, the variation is both quantitative and qualitative for different angles of incidence. Therefore, from analysis of Fig. 1, one can generally expect completely different spectral distortions for fibers compared to spherical samples.

Optimization of Extended Multiplicative Signal Correction Algorithm for Mie Scatterers

Although there are various optimizations and improvements of the EMSC algorithm for Mie scattering in terms of speed[51] and stability,[54] there is at least one possible improvement that has not been addressed so far. The original RMieS/EMSC algorithm[50] generates around $\simeq 1000$ permutations of Q_{sca} at each iteration step for each given data set which arises from various combinations of size, mean value of the refractive index, and its variation according to Kramers–Kroning relations. The use of the van de Hulst analytic solution for Q_{sca} does not significantly affect the performance of RMieS/EMSC in terms of speed and accuracy; however, the use of the EMSC extended for cylindrical particles requires significant computational resources because of the lack of a simple and accurate approximation for Q_{sca}. GPU-enabled calculations of the Bessel functions which enter Eqs. 3 and 4 may enhance the performance as shown in Bassan et al.[51] We propose that there is a way to avoid extensive calculations in this case. From Eqs. 3 and 4, along with expressions for expansion coefficients given in the Appendix, one can conclude that the only two parameters which contribute to Q_{sca}, the refractive index n_p and size parameter $x = 2\pi n_h \nu r$, describe possible permutations which arise from variations of ν and r. Thus, various combinations of ν and r may yield the same values of x for fixed n_h which is considered to be unity. Therefore, the large number of permutations of three variables can be shrunk to a smaller number (approximately by the order of
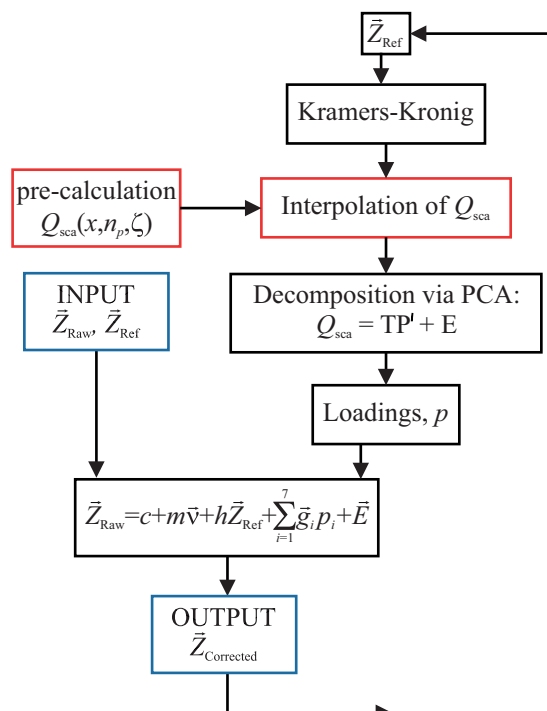
magnitude) while retaining the accuracy of the method. One more usually overlooked practical aspect in implementation is that these permutations are repeatedly calculated for almost the same set of x and n_p during iterations. Thus, it might be more practical and convenient to calculate the possible set of Q_{sca} before launching a RMieS/EMSC procedure. For each iteration step then, we propose to either find these values in pre-calculated data or perform an interpolation instead of calculating Q_{sca}. This approach, as detailed in the flow chart shown in Fig. 2, will be less computationally expensive compared to straightforward simulation of Q_{sca} with Eqs. 2–4 and is a significant, enabling step for large imaging data sets.

To demonstrate the utility of this concept, we have simulated the comprehensive Q_{sca} data set for a number of values of x and n_p that span the vast majority of possible parameters of polymeric and biological samples. The endmembers of our database comprise $x_{min} = 0.5$ and $x_{max} = 25$, which correspond to $(\nu = 800\,cm^{-1}, r = 1\,\mu m)$ and $(\nu = 4000\,cm^{-1}, r = 10\,\mu m)$, respectively. Thus, for commonly utilized bandwidth for IR spectral analyses, this size parameter covers the vast majority of combinations of frequency and radii of fibers. Simultaneously, the minimum and maximum real refractive index of the particle has been set to $n_{p,min} = 1$ and $n_{p,max} = 2.1$, respectively, which is once again spans the vast majority of polymeric and biological samples.

Figure 2. Flow chart illustrating the iterative procedure of the EMSC algorithm. Red boxes indicate the modifications to the original RMieS/EMSC procedure[50] proposed in this work.
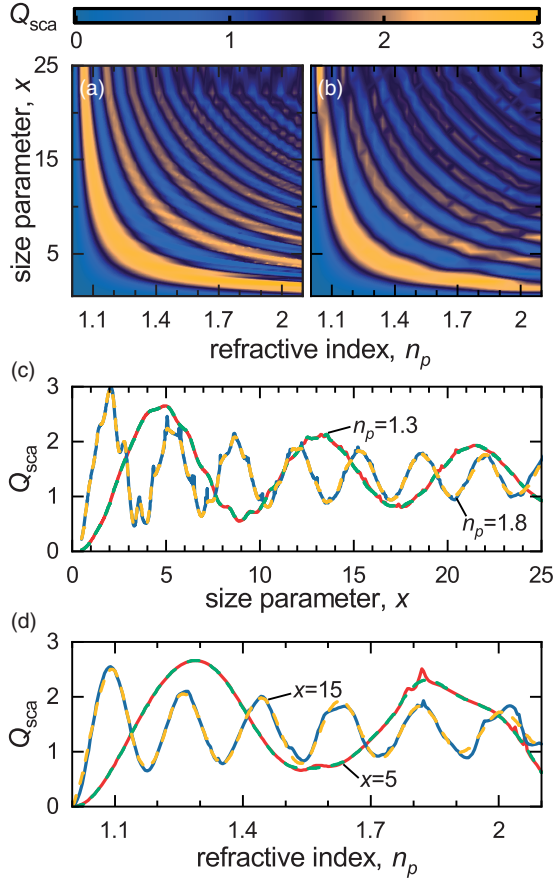
Figure 3. (a) Accurate calculation with fine mesh and (b) spline interpolation from coarse data for scattering efficiency Q_{sca} as a function of refractive index n_p and size parameter x for non-absorbing cylinder under unpolarized incident illumination impinging under $\zeta = 45°$ angle, and corresponding efficiency for fixed refractive index (c) and size parameter (d). Solid (red and blue) lines correspond to exact solution while dashed (green and yellow) lines represent interpolated data.

Figure 3a shows the calculated Q_{sca} on a fine grid of x and n_p (1577 × 232 points, respectively), while Fig. 3b shows Q_{sca} on the same range and grid of x and n_p but spline-interpolated from coarsely simulated data (122 × 23 points). It can be seen that interpolation of Q_{sca} reproduces most of the essential features of the actual curves. To get a deeper insight, we provide the cross-sections of Q_{sca} for fixed refractive index n_p and size parameter x, in Fig. 3c and 3d, respectively. The negligible discrepancy between precisely calculated scattering efficiency and obtained via interpolation arises only in $n_p > 1.7$ range for fixed x, while interpolated curves agree well with precise Q_{sca} for fixed n_p. Given that most real objects are not perfect cylinders, and even for perfect geometries the error will be small, we anticipate that the algorithm will be more than adequate in accuracy and a significant increase in computing speed for most applications.

Verification of Extended Multiplicative Signal Correction on Simulated Data

Finally, to verify the proposed modification of the EMSC procedure and to demonstrate its validity, we apply the developed algorithm to synthetic data. Figure 4a shows absorbance of a PMMA cylinder with $r = 5\,\mu m$ calculated with the rigorous forward model from Davis et al.[30] The condenser and detection optics are composed of Schwarzschild objectives with numerical apertures $NA_c = NA_d = 0.65$ and an obscuration with numerical apertures $NA_{cob} = NA_{dob} = 0.23$.

Scattering-free absorbance calculated in accordance with the Beer's law[30,41] has been chosen as the reference spectrum Z_{Ref} for the EMSC:

$$A = \frac{4\pi\tilde{\nu}kd_{eff}}{\log_e(10)} \tag{5}$$

where $d_{eff} = 4r/3$ is the effective thickness of the sample.[53]

It can be seen from comparing Fig. 4a and 4b that the recorded signal is significantly different from the ideal one given by Eq. 5, which is explained by the effects of scattering. To mitigate scattering, we implemented the EMSC procedure in the following manner: we limited the database with $x \in [3, 17]$ and $n_p \in [1.2, 1.6]$ and used 10 iterations. It can be seen from Fig. 4c that the effects of scattering are removed and the corrected absorbance coincides with the ideal case from Fig. 4b. However, as it might be expected, it is difficult to recover the signal at strongly absorbing bands near $\nu = 1728\,cm^{-1}$ and $\nu = 1152\,cm^{-1}$. For comparison, Fig. 4d also provides the absorbance calculated with Eq. 5 but for k recovered via iterative algorithm from Davis et al.[30] It can be seen from Fig. 4e and 4f that both EMSCs adapted for fibers, and the iterative algorithm from Davis et al.[30] provides reliable results with acceptable errors. However, the EMSC procedure can be easily applied for large data sets, while the formalism from Davis et al.[30] is only applicable to pixels located in the middle of fiber since it assumes a perfect cylindrical object. Thus, while the results of the EMSC algorithm are not as precise as an exact model, the EMSC algorithm is more generally applicable without need for constraints of geometry. We note that the approximations within the EMSC approach may not allow a perfect recovery, especially for strongly absorbing vibrational modes, but are considerably improved compared to the recorded data in Fig. 4a.

Experimental Methods

Samples

Two types of fibrous samples, fungi and cellulose fibers, were prepared to test the modified EMSC approach proposed in this study. For fungal samples, a filamentous fungal
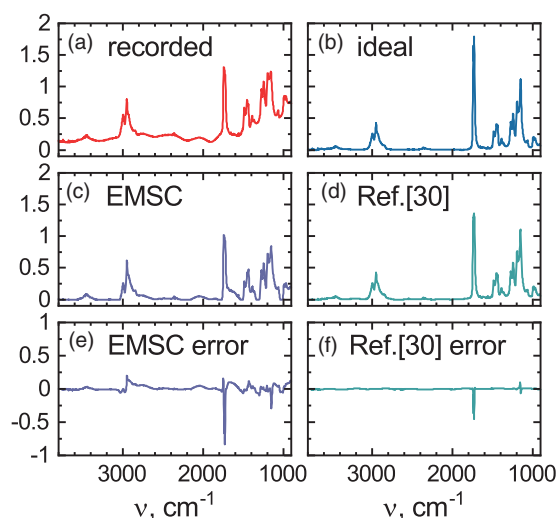
Figure 4. (a) Absorbance of PMMA cylinder with r = 5 μm calculated with forward model from Davis et al.[30] (b) Ideal scattering-free absorbance calculated with Eq. 5 and used as Z_{Ref} in Eq. 1. (c) EMSC-corrected absorbance and (d) absorbance calculated with Eq. 5 but for k recovered via iterative algorithm from Davis et al.[30] (e, f) Absolute errors between corrected and ideal absorbance for EMSC and iterative algorithm, respectively.

strain *Fusarium spp.* with pronounced cylinder-like shapes[62,63] were grown in petri dishes on potato dextrose agar (PDA) media incubated at 28 °C and 80% relative humidity. Fungal filaments (hyphae) that grew above the PDA surface were carefully picked and deposited on the top of low-E glass slides (Kevley Technologies) in such a way that the curved surfaces of these filaments lay horizontally on the low-E slides, shown in Fig. 5a. Similarly, cellulose samples were prepared by laying fibers from cellulose pad strips (MilliporeSigma, CFSP 173000) on a 4 mm thick rectangular BaF_2 window (Spectral Systems LLC.).

Data Acquisition

A Cary 620 FT-IR Microscope (Agilent Technologies) imaging system was used to collect FT-IR imaging data at 4 cm^{-1} spectral resolution (truncated to the detector sensitive range of 3800 cm^{-1} to 900 cm^{-1} wavenumbers) and 5.5 × 5.5 μm^2 per pixel spatial resolution using 15 × (NA = 0.62) magnification objective in standard definition mode. For each image, spectra were collected using identical spectral and spatial parameters with 128 spectral co-additions for background and 64 co-additions for the sample. In total, 16 384 spectra per image were collected in a 704 × 704 μm^2 (128 × 128 pixel^2) area. For both types of samples, similar parameters were used for FT-IR data collection except the fungal sample was imaged in transflection mode while the cellulose sample was imaged in transmission mode. The optical microscopy image for fungi shown in Fig. 5a was captured using the same FT-IR microscopy setup in reflection mode, while the optical image for

cellulose sample shown in Fig. 5b was collected on Zeiss Axio Imager M2 microscopy system with the 10 × (NA = 0.3) objective in transmission mode. We note that the choice of different substrates both for transflection and transmission modes might affect the recorded signal; however, for sufficiently large samples, this effect is almost negligible for the transflection regime,[34] and one could expect the same trend for transmission mode.

Data Analysis

Before the modified EMSC algorithm was applied, a minimum noise fraction (MNF)[64] preprocessing was performed on the collected FT-IR data for noise reduction using Environment for Visualization (ENVI)-Interactive Data Language (IDL) version 4.8. The MNF corrected data were processed with the modified RMieS/EMSC procedure adapted and optimized for cylinder-shape samples from original RMieS/EMSC Matlab code.[65] The modified algorithm was implemented in Matlab (Mathworks, Inc., Version 2018a) environment and tested on a desktop computer equipped with an Intel Core i7-6920HQ CPU @ 2.90 GHz processor. The pre-calculation of Q_{sca} database on a fine grid with 4 cm^{-1} spectral resolution takes up to several minutes, while the interpolation procedure using default Matlab functions requires < 50 ms for each iteration, depending on the number of permutations. Post-processing of 1 pixel of data requires ∼ 500 ms per iteration; thus, as might be expected, PCA takes most of the computational time.

Results and Discussion

As mentioned previously, the main utility of the EMSC algorithm lies in the generalized analysis of spectra from complex samples in an image. We demonstrate the applicability of our approach to two complex samples, namely fungi and fibrous cellulose. Fungi have been analyzed extensively by IR microscopy[66–72] and previous attempts at correcting data used the formulation of the EMSC that did not take into account the actual shape of the sample. Here, we apply the cylindrical version developed in this study, which is more suitable for the morphology.

The individual hyphae diameters are in the approximate range of 2–6.5 μm. However, in most of the cases, a collection of hyphae forms a bundle with diameters up to 25 μm. For given spatial resolution, each hyphae within the bundle might be considered as a single fiber. The diameter of each individual cellulose fiber is in the range of 6–20 μm. The size parameters shown in Fig. 3 cover all of these possible variations for the whole spectral range; therefore, we have used this pre-calculated set of Q_{sca} for the EMSC procedure. As a reference spectrum, we have chosen the data recorded from the densest parts of the sample both for fungi and cellulose, assuming that the relative scattering
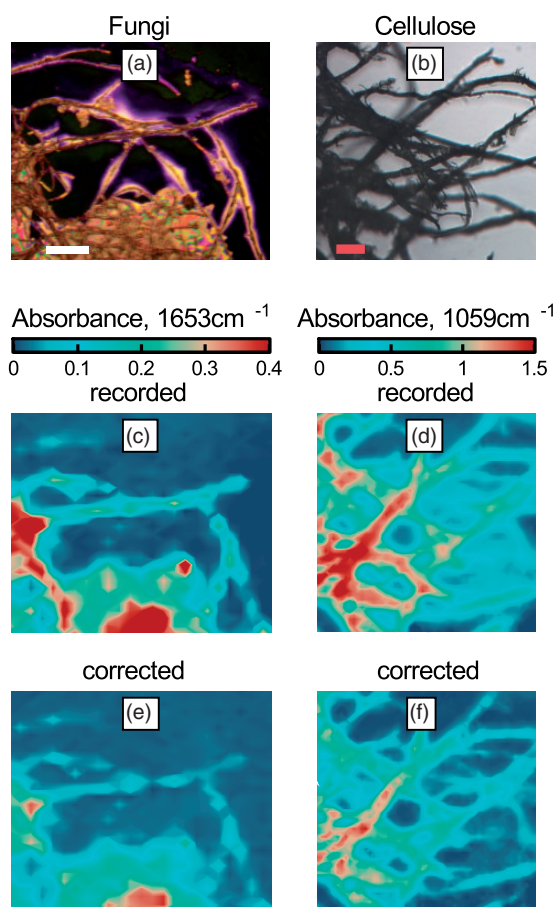
Fungi

Cellulose

Absorbance, 1653cm^{-1}

Absorbance, 1059cm^{-1}

| 0 | 0.1 | 0.2 | 0.3 | 0.4 |

| 0 | 0.5 | 1 | 1.5 |

recorded

recorded

corrected

corrected

Figure 5. (a) Optical reflection microscopy image of filamentous structures hyphae from fungal strain *Fusarium spp.* onto a reflective low-E glass slide for IR imaging. The lower and left dense parts show hyphae mixed with PDA media. Scale bar: 100 μm. (b) Cellulose fibers images acquired in the transmission mode. Scale bar: 100 μm. (c, d) Recorded absorbance at $\vec{v} = 1653 \, cm^{-1}$ and $\vec{v} = 1059 \, cm^{-1}$. (e, f) The same data after applying EMSC adapted for fibers.

contribution is minimal in these cases.[40] Each pixel of the measured data has been processed via EMSC with 10 iterations.

The images before and after correction, shown in Fig. 5c and 5e for fungi and in Fig. 5d and 5f for cellulose, demonstrate changes in several regions. The recorded data become more consistent after application of the scattering correction and increased contrast is clearly seen for regions where fiber-like samples are located. We note that fibers not in the plane of focus within these samples are blurred and may be difficult to visualize in the IR images, compared to the optical microscopy image. This is especially true of the samples on reflective slides (e.g., fungi here). In both cases, the images reflect the corrections in the underlying spectra. As expected from our results on synthetic data, a major manifestation in the correction is the mitigation of scattering-induced baseline offsets in

individual spectra, as can be seen in Fig. 6. Examining spectra from the respective images shows that, indeed, EMSC successfully reduces the effect of scattering as seen in spectra gathered from samples with pronounced cylinder shapes in both cases. The question of precisely recovering band shapes is more complex and there are several confounding factors. First, the downside of wide and easy applicability to entire images is that pixels may be addressed that do not capture the entire scattering profile of a fiber. Second, in complex samples of the type seen in the two examples here, multiple scattering and focusing may also play a role that cannot be captured by EMSC. It should be recognized that there are no methods available to entirely correct spectra from arbitrary number of these effects. We note that the success of our implementation does include a mitigation of scattering induced baseline variations and accurate appearing spectra.

We compared our corrected spectra to those reported in other studies, though we caution that comparing single fibers is much easier than comparing spectra from complicated mixtures of cylindrical objects at varying density in an imaging plane, as attempted here. In general, the major spectra line shapes and peak positions agree well with typical spectra previously reported for both cases. For example, cellulose spectra for cotton fluff reported in the study by Zhbankov[73] show prominent features around $2950 \, cm^{-1}$ and $3300 \, cm^{-1}$, which are also observed in Fig. 6b and 6d. However, we note that the peak at $3300 \, cm^{-1}$ for corrected spectra is sharper than that reported in the literature. While the scattering correction works well in removing baseline variations, the strongly absorbing region of the high wavenumber region does not agree as well. This observation is consistent with our synthetic data in which strongly absorbing regions of the PMMA spectrum were not easily corrected. Moreover, the same trend for peaks at the $v > 3000 \, cm^{-1}$ spectral region has already been observed in Bassan et al.[50] for EMSC of biological samples. The primary effect of baseline offset correction and the consistency of spectra from different parts of the sample is highly encouraging as there is no reason to expect any variation in the actual absorbance of individual spectra. The result underscores the major benefit of the EMSC algorithm and its application here in that the method corrects spectra from heterogeneous samples which is otherwise not possible. Figure 6c shows that our corrected fungi spectra also agree well with the comprehensive data recently reported in Kosa et al.[70] in broad terms. One could clearly observe the spectral features due to the presence of lipids (around $2900 \, cm^{-1}$ and $1400 \, cm^{-1}$), proteins (around $1600 \, cm^{-1}$), sugars, and phosphates (around $1200–1100 \, cm^{-1}$). Once again, however, precise comparisons between each filament's true spectrum and the corrected one is difficult to verify in these samples. There is more variation in the corrected spectra of fungi as opposed to that in cellulose fibers. This might be expected
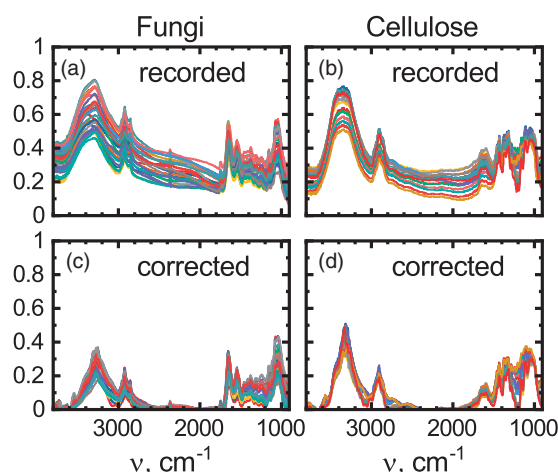
Figure 6. Recorded (top) and corrected (bottom) absorbance for fungi (left) and cellulose (right) samples. Spectra are recorded from 30 pixels containing samples with a pronounced cylinder-like shape.

from biological variations in composition and shape as there seems to be little other reason why the corrections would perform any differently from the cellulose case. The limitations in both these cases may arise from the limited extent of scattered light captured by the optical system at every pixel, multiple scattering from overlapped fibrous material, preparation or biologic variation, and variations in geometric parameters – all of which are to be expected in complex samples. Finally, the samples themselves are highly heterogeneous – from single fibers to almost a bulk-like composition. Despite these variations and complications, the utility of the EMSC algorithm in application is a major benefit while consistency of spectra and elimination of baseline offsets due to scattering are remarkable.

It is noteworthy that recently developed improvements (in terms of stability, convergence, and overall performance) of EMSC for spherical samples might be also applied for fibers, e.g., characterizing the sample by the effective optical path length instead of its radius[53] or optimizing the number of iterations and principal components used in Eq. 1.[54] These strategies require comprehensive benchmarks which are beyond the scope of this paper. Together, these advances and the rigorous basis of extension to fibers proposed here can greatly accelerate the development of better algorithms as well as further testing and use for IR imaging of heterogeneous samples containing cylindrical domains.

Conclusion

In this study, we have proposed a modified version of the extended multiplicative signal correction procedure for IR spectroscopy that specifically addresses cylindrical-shaped samples and domains in heterogeneous materials. In order to utilize rigorous Mie theory for calculation of the

scattering efficiency of the infinite cylinder further, we have proposed to change the usual workflow of the EMSC algorithm. Namely, instead of estimating the large number of permutations of Q_{sca} at each iteration step for each recorded curve, we propose calculating the set of possible Q_{sca} before launching the EMSC procedure. Interestingly, this approach arises from rigorous theoretical analysis and allows us to decrease the number of variables entering the calculation of Q_{sca}: from the usually utilized three (wavenumber ν, radius r, and refractive index n_p) to two (size parameter x and refractive index n_p), which further reduces the computational complexity of EMSC. We tested our method with synthetic data formulated from a rigorous forward model of fibers. The correction is shown to work well for most regions of the spectrum but less than optimal from a rigorous analytical solution of a perfectly shaped and centered (in the microscope) cylinder. Finally, we demonstrated the application of the modified and optimized EMSC algorithm to data recorded from polymers and fungi. The pronounced effects arising from scattering were successfully removed. Mitigating the effects of scattering from recorded absorption spectra improves the reliability of the analysis from fiber-shaped objects or cylindrical domains in samples and leads to improved analytical capability that is generally applicable in different applications spanning materials science, forensics, and biological domains.

Conflict of Interest

The authors report there are no conflicts of interest.

ORCID iD

Ilia L. Rasskazov ⓘ http://orcid.org/0000-0002-7956-1702
Rohit Bhargava ⓘ http://orcid.org/0000-0001-7360-994X

References

1. R. Bhargava. "Infrared Spectroscopic Imaging: The Next Generation". Appl. Spectrosc. 2012. 66(10): 1091–1120.
2. M.J. Baker, J. Trevisan, P. Bassan, et al. "Using Fourier Transform IR Spectroscopy to Analyze Biological Materials". Nat. Protoc. 2014. 9(8): 1771–1791.
3. K.L. Andrew Chan, S.G. Kazarian. "Attenuated Total Reflection Fourier-Transform Infrared (ATR-FTIR) Imaging of Tissues and Live Cells". Chem. Soc. Rev. 2016. 45(7): 1850–1864.
4. J.A. Kimber, L. Foreman, B. Turner, et al. "FTIR Spectroscopic Imaging and Mapping with Correcting Lenses for Studies of Biological Cells and Tissues". Faraday Discuss. 2016. 187(0): 69–85.
5. J. De Meutter, J. Vandenameele, A. Matagne, et al. "Infrared Imaging of High Density Protein Arrays". Analyst. 2017. 142(8): 1371–1380.
6. T.P. Wrobel, R. Bhargava. "Infrared Spectroscopic Imaging Advances as an Analytical Technology for Biomedical Sciences". Anal. Chem. 2018. 90(3): 1444–1463.
7. J.L. Koenig. Spectroscopy of Polymers, 2nd ed. Cleveland, OH: Elsevier, 1999.

8. S.G. Kazarian, K.L. Andrew Chan. "FTIR Imaging of Polymeric Materials Under High-Pressure Carbon Dioxide". Macromolecules. 2004. 37(2): 579–584.

9. M. Lopes, V. Mouillet, L. Bernucci, et al. "The Potential of Attenuated Total Reflection Imaging in the Mid-Infrared for the Study of Recycled Asphalt Mixtures". Constr. Build. Mater. 2016. 124: 1120–1131.

10. E.G. Bartick, M.W. Tungol, J.A. Reffner. "A New Approach to Forensic Analysis with Infrared Microscopy: Internal Reflection Spectroscopy". Anal. Chim. Acta. 1994. 288(1–2): 35–42.

11. A.V. Ewing, S.G. Kazarian. "Infrared Spectroscopy and Spectroscopic Imaging in Forensic Science". Analyst. 2017. 142(2): 257–272.

12. T. Victor, N. Delpratt, S.B. Cseke, et al. "Imaging Nutrient Distribution in the Rhizosphere Using FTIR Imaging". Anal. Chem. 2017. 89(9): 4831–4837.

13. S. Türker-Kaya, C. Huck. "A Review of Mid-Infrared and Near-Infrared Imaging: Principles, Concepts and Applications in Plant Tissue Analysis". Molecules. 2017. 22(1): 168.

14. V. Turzhitsky, L. Qiu, I. Itzkan, et al. "Spectroscopy of Scattered Light for the Characterization of Micro and Nanoscale Objects in Biology and Medicine". Appl. Spectrosc. 2014. 68(2): 133–154.

15. J.T. Kwak, A. Kajdacsy-Balla, V. Macias, et al. "Improving Prediction of Prostate Cancer Recurrence Using Chemical Imaging". Sci. Rep. 2015. 5: 8758.

16. V. Bobroff, H.H. Chen, M. Delugin, et al. "Quantitative IR Microscopy and Spectromics Open the Way to 3D Digital Pathology". J. Biophotonics. 2017. 10(4): 598–606.

17. J.T. Kwak, S.M. Hewitt, A.A. Kajdacsy-Balla, et al. "Automated Prostate Tissue Referencing for Cancer Detection and Diagnosis". BMC Bioinf. 2016. 17(1): 227.

18. J. Nallala, G.R. Lloyd, M. Hermes, et al. "Enhanced Spectral Histology in the Colon Using High-Magnification Benchtop FTIR Imaging". Vib. Spectrosc. 2017. 91: 83–91.

19. H. Sreedhar, V.K. Varma, F.V. Gambacorta, et al. "Infrared Spectroscopic Imaging Detects Chemical Modifications in Liver Fibrosis due to Diabetes and Disease". Biomed. Opt. Express. 2016. 7(6): 2419.

20. S. Tiwari, J. Raman, V. Reddy, et al. "Towards Translation of Discrete Frequency Infrared Spectroscopic Imaging for Digital Histopathology of Clinical Biopsy Samples". Anal. Chem. 2016. 88(20): 10183–10190.

21. I. Zawlik, E. Kaznowska, J. Cebulski, et al. "FPA-FTIR Microspectroscopy for Monitoring Chemotherapy Efficacy in Triple-Negative Breast Cancer". Sci. Rep. 2016. 6(1): 37333.

22. F. Großerueschkamp, T. Bracht, H.C. Diehl, et al. "Spatial and Molecular Resolution of Diffuse Malignant Mesothelioma Heterogeneity by Integrating Label-Free FTIR Imaging, Laser Capture Microdissection and Proteomics". Sci. Rep. 2017. 7(1): 44829.

23. A.D. Surowka, M. Pilling, A. Henderson, et al. "FTIR Imaging of the Molecular Burden Around Aβ Deposits in an Early-Stage 3-Tg-APP-PSP1-TAU Mouse Model of Alzheimer's Disease". Analyst. 2017. 142(1): 156–168.

24. A. Sarkar, S. Sengupta, A. Mukherjee, et al. "Fourier Transform Infra-Red Spectroscopic Signatures for Lung Cells' Epithelial Mesenchymal Transition: A Preliminary Report". Spectrochim. Acta, Part A. 2017. 173: 809–816.

25. S. Pahlow, K. Weber, J. Popp, et al. "Application of Vibrational Spectroscopy and Imaging to Point-of-Care Medicine: A Review". Appl. Spectrosc. 2018. 72(S1): 52–84.

26. M. Miljković, B. Bird, M. Diem. "Line Shape Distortion Effects in Infrared Spectroscopy". Analyst. 2012. 137(17): 3954.

27. R. Bhargava, S.Q. Wang, J.L. Koenig. "FT-IR Imaging of the Interface in Multicomponent Systems Using Optical Effects Induced by Differences in Refractive Index". Appl. Spectrosc. 1998. 52(3): 323–328.

28. P. Bassan, H.J. Byrne, F. Bonnier, et al. "Resonant Mie Scattering in Infrared Spectroscopy of Biological Materials - Understanding the "Dispersion Artefact"". Analyst. 2009. 134(8): 1586.

29. S. Berisha, T. van Dijk, R. Bhargava, et al. "BIM-Sim: Interactive Simulation of Broadband Imaging Using Mie Theory". Front. Phys. 2017. 5: 5.

30. B.J. Davis, P.S. Carney, R. Bhargava. "Theory of Infrared Microspectroscopy for Intact Fibers". Anal. Chem. 2011. 83(2): 525–532.

31. P. Bassan, J. Lee, A. Sachdeva, et al. "The Inherent Problem of Transflection-Mode Infrared Spectroscopic Microscopy and the Ramifications for Biomedical Single Point and Imaging Applications". Analyst. 2013. 138(1): 144–157.

32. T.P. Wrobel, B. Wajnchold, H.J. Byrne, et al. "Electric Field Standing Wave Effects in FT-IR Transflection Spectra of Biological Tissue Sections: Simulated Models of Experimental Variability". Vib. Spectrosc. 2013. 69: 84–92.

33. E. Staniszewska-Slezak, A. Rygula, K. Malek, et al. "Transmission Versus Transflection Mode in FTIR Analysis of Blood Plasma: Is the Electric Field Standing Wave Effect the Only Reason for Observed Spectral Distortions?" Analyst. 2015. 140(7): 2412–2421.

34. B.M. DeVetter, S. Kenkel, S. Mittal, et al. "Characterization of the Structure of Low-e Substrates and Consequences for IR Transflection Measurements". Vib. Spectrosc. 2017. 91: 119–127.

35. J. Lee. "On the Non-Existence of the So-Called "Electric Field Standing Wave Effect" in Transflection FTIR Spectra". Vib. Spectrosc. 2017. 90: 104–111.

36. T.G. Mayerhöfer, H. Mutschke, J. Popp. "The Electric Field Standing Wave Effect in Infrared Transmission Spectroscopy". ChemPhysChem. 2017. 18(20): 2916–2923.

37. T.G. Mayerhöfer, J. Popp. "The Electric Field Standing Wave Effect in Infrared Transflection Spectroscopy". Spectrochim. Acta, Part A. 2018. 191: 283–289.

38. B.J. Davis, P.S. Carney, R. Bhargava. "Theory of Midinfrared Absorption Microspectroscopy: I. Homogeneous Samples". Anal. Chem. 2010. 82(9): 3474–3486.

39. B.J. Davis, P.S. Carney, R. Bhargava. "Theory of Mid-infrared Absorption Microspectroscopy: II. Heterogeneous Samples". Anal. Chem. 2010. 82(9): 3487–3499.

40. I.L. Rasskazov, N. Spegazzini, P.S. Carney, et al. "Dielectric Sphere Clusters as a Model to Understand Infrared Spectroscopic Imaging Data Recorded from Complex Samples". Anal. Chem. 2017. 89(20): 10813–10818.

41. T. van Dijk, D. Mayerich, P.S. Carney, et al. "Recovery of Absorption Spectra from Fourier Transform Infrared (FT-IR) Microspectroscopic Measurements of Intact Spheres". Appl. Spectrosc. 2013. 67(5): 546–552.

42. R. Lukacs, R. Blümel, B. Zimmerman, et al. "Recovery of Absorbance Spectra of Micrometer-Sized Biological and Inanimate Particles". Analyst. 2015. 140(9): 3273–3284.

43. R. Blümel, M. Bağcioğlu, R. Lukacs, et al. "Infrared Refractive Index Dispersion of Polymethyl Methacrylate Spheres from Mie Ripples in Fourier-Transform Infrared Microscopy Extinction Spectra". J. Opt. Soc. Am. A. 2016. 33(9): 1687.

44. T. Konevskikh, A. Ponossov, R. Blümel, et al. "Fringes in FTIR Spectroscopy Revisited: Understanding and Modelling Fringes in Infrared Spectroscopy of Thin Films". Analyst. 2015. 140(12): 3969–3980.

45. T. Mayerhöfer, S. Pahlow, U. Hübner, et al. "Removing Interference-Based Effects from the Infrared Transflectance Spectra of Thin Films on Metallic Substrates: A Fast and Wave Optics Conform Solution". Analyst. 2018. 143(13): 3164–3175.

46. A. Dazzi, A. Deniset-Besseau, P. Lasch. "Minimising Contributions from Scattering in Infrared Spectra by Means of an Integrating Sphere". Analyst. 2013. 138(14): 4191.

47. J.G. Gwon, S.Y. Lee, G.H. Doh, et al. "Characterization of Chemically Modified Wood Fibers Using FTIR Spectroscopy for Biocomposites". J. Appl. Polym. Sci. 2010. 116(6): 3212–3219.

48. A. Kohler, U. Böcker, J. Warringer, et al. "Reducing Inter-Replicate Variation in Fourier Transform Infrared Spectroscopy by Extended Multiplicative Signal Correction". Appl. Spectrosc. 2009. 63(3): 296–305.

49. A. Kohler, J. Sulé-Suso, G.D. Sockalingum, et al. "Estimating and Correcting Mie Scattering in Synchrotron-Based Microscopic Fourier Transform Infrared Spectra by Extended Multiplicative Signal Correction". Appl. Spectrosc. 2008. 62(3): 259–266.

50. P. Bassan, A. Kohler, H. Martens, et al. "Resonant Mie Scattering (RMieS) Correction of Infrared Spectra from Highly Scattering Biological Samples". Analyst. 2010. 135(2): 268–277.

51. P. Bassan, A. Kohler, H. Martens, et al. RMieS-EMSC Correction for Infrared Spectra of Biological Cells: Extension Using Full Mie Theory and GPU Computing". J. Biophotonics. 2010. 3(8–9): 609–620.

52. B. Bird, M. Miljković, M. Diem. "Two Step Resonant Mie Scattering Correction of Infrared Micro-Spectral Data: Human Lymph Node Tissue". J. Biophotonics. 2010. 3(8-9): 597–608.

53. T. Konevskikh, R. Lukacs, R. Blümel, et al. "Mie Scatter Corrections in Single Cell Infrared Microspectroscopy". Faraday Discuss. 2016. 187: 235–257.

54. T. Konevskikh, R. Lukacs, A. Kohler. "An Improved Algorithm for Fast Resonant Mie Scatter Correction of Infrared Spectra of Cells and Tissues". J. Biophotonics. 2018. 11(1): e201600307.

55. P. Bassan, A. Sachdeva, A. Kohler, et al. "FTIR Microscopy of Biological Cells and Tissue: Data Analysis Using Resonant Mie Scattering (RMieS) EMSC Algorithm". Analyst. 2012. 137(6): 1370.

56. H. Martens, J.P. Nielsen, S.B. Engelsen. "Light Scattering and Light Absorbance Separated by Extended Multiplicative Signal Correction. Application to Near-Infrared Transmission Analysis of Powder Mixtures". Anal. Chem. 2003. 75(3): 394–404.

57. A. Kohler, C. Kirschner, A. Oust, et al. "Extended Multiplicative Signal Correction as a Tool for Separation and Characterization of Physical and Chemical Information in Fourier Transform Infrared Microscopy Images of Cryo-Sections of Beef Loin". Appl. Spectrosc. 2005. 59(6): 707–716.

58. N.K. Afseth, A. Kohler. "Extended Multiplicative Signal Correction in Vibrational Spectroscopy, a Tutorial". Chemom. Intell. Lab. Syst. 2012. 117: 92–99.

59. H.C. van de Hulst. Light Scattering by Small Particles. New York: John Wiley and Sons, 1957.

60. A. Walter, S. Erdmann, T. Bocklitz, et al. "Analysis of The Cytochrome Distribution via Linear and Nonlinear Raman Spectroscopy". Analyst. 2010. 135(5): 908.

61. S. Oprea, P. Gradinariu, A. Joga, et al. "Fungal Degradation Behavior of Two Series of Polyurethane Urea Composites Obtained by Different Silver Incorporation Methods". J. Elastomers Plast. 2017. 49(2): 120–131.

62. M. Papagianni. "Fungal Morphology and Metabolite Production in Submerged Mycelial Processes". Biotechnol. Adv. 2004. 22(3): 189–259.

63. R. Trabelsi, H. Sellami, Y. Gharbi, et al. "Morphological and Molecular Characterization of Fusarium Spp. Associated with Olive Trees Dieback in Tunisia". 3 Biotech. 2017. 7(1): 28.

64. R.K. Reddy, R. Bhargava. Accurate Histopathology from Low Signal-to-Noise Ratio Spectroscopic Imaging Data". Analyst. 2010. 135(11): 2818.

65. P. Bassan, A. Kohler, H. Martens, et al. "Resonant Mie Scattering EMSC (RMieS-EMSC) Correction for Infrared Spectroscopy". 2017. https://github.com/GardnerLabUoM/RMieS [accessed Mar 15 2019].

66. A. Szeghalmi, S. Kaminskyj, K.M. Gough. "A Synchrotron FTIR Microspectroscopy Investigation of Fungal Hyphae Grown Under Optimal and Stressed Conditions". Anal. Bioanal. Chem. 2007. 387(5): 1779–1789.

67. K. Jilkine, K.M. Gough, R. Julian, et al. "A Sensitive Method for Examining Whole-Cell Biochemical Composition in Single Cells of

68. Filamentous Fungi Using Synchrotron FTIR Spectromicroscopy". J. Inorg. Biochem. 2008. 102(3): 540–546.

68. J.D. Pallua, W. Recheis, R. Pöder, et al. "Morphological and Tissue Characterization of the Medicinal Fungus Hericium Coralloides by a Structural and Molecular Imaging Platform". Analyst. 2012. 137(7): 1584–1595.

69. A. Naumann. "Fourier Transform Infrared (FTIR) Microscopy and Imaging of Fungi". In: T.E.S. Dahms, K.J. Czymmek, editors. Advanced Microscopy in Mycology. Cham: Springer, 2015. pp.61–88.

70. G. Kosa, A. Kohler, V. Tafintseva, et al. "Microtiter Plate Cultivation of Oleaginous Fungi and Monitoring of Lipogenesis by High-Throughput FTIR Spectroscopy". Microb. Cell Fact. 2017. 16(1): 101.

71. J. Piekarczyk, H. Ratajkiewicz, J. Jasiewicz, et al. An Application of Reflectance Spectroscopy to Differentiate of Entomopathogenic Fungi Species". J. Photochem. Photobiol. B. 2018. 190: 32–41.

72. K. Wang, H. Pu, D.W. Sun. "Emerging Spectroscopic and Spectral Imaging Techniques for the Rapid Detection of Microorganisms: An Overview". Compr. Rev. Food Sci. Food Saf. 2018. 17(2): 256–273.

73. R.G. Zhbankov. "Model Cellulose Compounds. Unmodified Celluloses". In: R.G. Zhbankov, editor. Infrared Spectra of Cellulose and Its Derivatives. Boston, MA: Springer US, 1995. pp.35–71.

74. C.F. Bohren, D.R. Huffman. Absorption and Scattering of Light by Small Particles. Weinheim, Germany: Wiley-VCH Verlag GmbH, 1998.

75. F. Frezza, F. Mangini, N. Tedeschi. "Introduction to Electromagnetic Scattering: Tutorial". J. Opt. Soc. Am. A. 2018. 35(1): 163.

76. J.R. Allardice, E.C. Le Ru. "Convergence of Mie Theory Series: Criteria for Far-Field and Near-Field Properties". Appl. Opt. 2014. 53(31): 7224.

Appendix

The exact solution for electromagnetic radiation scattering from dielectric spheres and infinite cylinders is extensively discussed in the literature and can be found elsewhere.[74,75] In this Appendix, we provide explicit equations for the reader's convenience.

Scattering efficiency of a spherical particle with radius r embedded in a host medium with real refractive index n_h is explicitly defined as follows:[74]

$$Q_{sca} = \frac{2}{x^2} \sum_{l=1}^{\infty} (2l+1)\left(|a_l|^2 + |b_l|^2\right) \tag{6}$$

Here $x = 2\pi n_h \nu r$ is a dimensionless size parameter and l is the order of a spherical harmonic. Coefficients a_l and b_l are explicitly defined by:

$$a_l = \frac{\tilde{n}^2 j_l(\tilde{n}x_i)[xj_l(x)]' - j_l(x)[\tilde{n}xj_l(\tilde{n}x)]'}{\tilde{n}^2 j_l(\tilde{n}x)\left[xh_l^{(1)}(x)\right]' - h_l^{(1)}(x)[\tilde{n}xj_l(\tilde{n}x)]'} \tag{7}$$

$$b_l = \frac{j_l(\tilde{n}x)[xj_l(x)]' - j_l(x)[\tilde{n}xj_l(\tilde{n}x)]'}{j_l(\tilde{n}x)\left[xh_l^{(1)}(x)\right]' - h_l^{(1)}(x)[\tilde{n}xj_l(\tilde{n}x)]'} \tag{8}$$

where $\tilde{n} = n_p/n_h$ is the refractive index of a sphere normalized with the respect to the surrounding medium with n_h; j_l and $h_l^{(1)}$ are spherical Bessel and spherical Hankel functions of the first kind, respectively, and prime denotes differentiation with respect to the argument in parentheses. Note that we set magnetic permeability to unity that is valid for non-magnetic biological tissues.

Coefficients a_l and b_l in Eqs. 3 and 4 for illumination with polarization parallel $\parallel$ and orthogonal $\perp$ to the cylinder axis of symmetry are defined as follows:

$$a_{l,\parallel} = \frac{C_l V_l - B_l D_l}{W_l V_l + i D_l^2}, \qquad b_{l,\parallel} = \frac{W_l B_l + i D_l C_l}{W_l V_l + i D_l^2}$$

$$a_{l,\perp} = -\frac{A_l V_l - i C_l D_l}{W_l V_l + i D_l^2}, \qquad b_{l,\perp} = -i \frac{C_l W_l + A_l D_l}{W_l V_l + i D_l^2}$$

(9)

$$A_l = i\xi\left[\xi J_l'(\eta) J_l(\xi) - \eta J_l(\eta) J_l'(\xi)\right]$$

$$B_l = \xi\left[\tilde{n}^2 \xi J_l'(\eta) J_l(\xi) - \eta J_l(\eta) J_l'(\xi)\right]$$

$$C_l = l \cos\zeta \eta J_l(\eta) J_l(\xi)\left(\frac{\xi^2}{\eta^2} - 1\right)$$

$$D_l = l \cos\zeta \eta J_l(\eta) H_l^{(1)}(\xi)\left(\frac{\xi^2}{\eta^2} - 1\right)$$

$$V_l = \xi\left[\tilde{n}^2 \xi J_l'(\eta) H_l^{(1)}(\xi) - \eta J_l(\eta) H_l^{(1)'}(\xi)\right]$$

$$W_l = i\xi\left[\eta J_l(\eta) H_l^{(1)'}(\xi) - \xi J_l'(\eta) H_l^{(1)}(\xi)\right]$$

where J_l and $H_l^{(1)}$ are Bessel and Hankel functions of the first kind, respectively; $\xi = \tilde{x}\sin\zeta$, $\eta = \tilde{x}\sqrt{\tilde{n}^2 - \cos^2\zeta}$, and $\tilde{x} = 2\pi\nu r$.

Finally, the upper limit l_{max} of summations in Eqs. 3–6 depends on the convergence criterion which might be different for each particular case of interest.[76] However, commonly utilized criterion is

$$l_{max} = x + 4.05x^{1/3} + 2 \tag{10}$$

for both spherical and cylindrical particles.